Inverse Monte Carlo as a Unified Reconstruction Algorithm for ECT

Carey E. Floyd Jr., Ronald J. Jaszczak, Kim L. Greer, and R. Edward Coleman

Department of Radiology, Duke University Medical Center, Durham, North Carolina

Tomographic reconstruction for single photon emission computed tomography (SPECT) with simultaneous compensation for attenuation, scatter, and distance dependent collimator resolution is provided by an Inverse Monte Carlo (IMOC) reconstruction algorithm. A detection probability matrix is formed by Monte Carlo solution to the photon transport equation for SPECT acquisition from a unit source activity in each reconstruction source voxel. The measured projection vector will equal the product of this detection probability matrix with the unknown source distribution vector. The resulting large, nonsparse system of equations is solved for the source distribution using an iterative Maximum Likelihood EM estimator. Reconstruction of experimentally acquired projections from phantoms shows quantitative compensation for scatter and attenuation. Comparison with filtered backprojection (FBP) reconstruction shows an improvement in resolution recovery, contrast, and signal-to-noise for the IMOC algorithm. Reconstruction of clinical studies shows improved contrast, structural resolution, and noise characteristics.

T he goal of quantitative emission computed tomography (ECT) is to determine the concentration of photon emitting radiopharmaceuticals within a body from measurements of the photon flux exterior to the body. Historically, a solution to the general mathematic problem presented by transaxial tomographic reconstruction was presented by Radon in 1917 (*1*). While a filtered backprojection technique was applied to radioastronomy imaging as early as 1957 (*2*), Kuhl and Edwards (*3,4*) were the first to apply the technique for reconstructing source distributions to single photon emission computed tomography (SPECT). Filtered backprojection (FBP) (*5–7*) is commonly used as the reconstruction algorithm for SPECT, although several iterative algebraic techniques have been proposed (*8–12*). The convolution-based FBP algorithm models ECT as a Radon transformation of the source space (unknown activity distribution) into a projection space (measured photon projections). The sampled projection space is transformed into an estimate of the source space by application of the inverse Radon transformation, usually performed using Fourier techniques. While FBP provides a computationally efficient reconstruction technique which lends itself to standard linear systems

analysis (*13–15*), the algorithm is based on a simple, idealized model of ECT and neglects important physical characteristics which are inherent in the acquisition of clinical data. More complete modeling of ECT acquisition in a typical clinical setting forms the basis for Inverse Monte Carlo (IMOC), a new unified algorithm for ECT reconstruction which includes simultaneous compensation for scatter, attenuation, and collimator divergence (*16*).

In the idealized Radon transform model of SPECT, depicted in Fig. 1, the acquired projection at a position x' on the face of the camera oriented at angle θ, is given by the line integral along the path through the activity distribution S(x,y). There are several implicit assumptions in this representation of an ECT projection. First, the line integral form assumes that the observed flux at the point x' on the detector is only due to activity along the infinitesimally narrow line. This condition is equivalent to assuming perfect collimation with no divergence and requires that there be no spatial spread in the crystal as well as no collimator penetration. Second, the line integral assumes no photon attenuation within the body. Third, this model assumes no scatter since all contributing source elements are assumed to lie on the line. While there do exist algorithms for attenuation and scatter which may be used with FBP (*17–22*), in all of these techniques the two compensations are performed sequentially rather than simultaneously and all

$$P(X',\theta) = \int S(x,y) \, d\alpha(X',\theta)$$
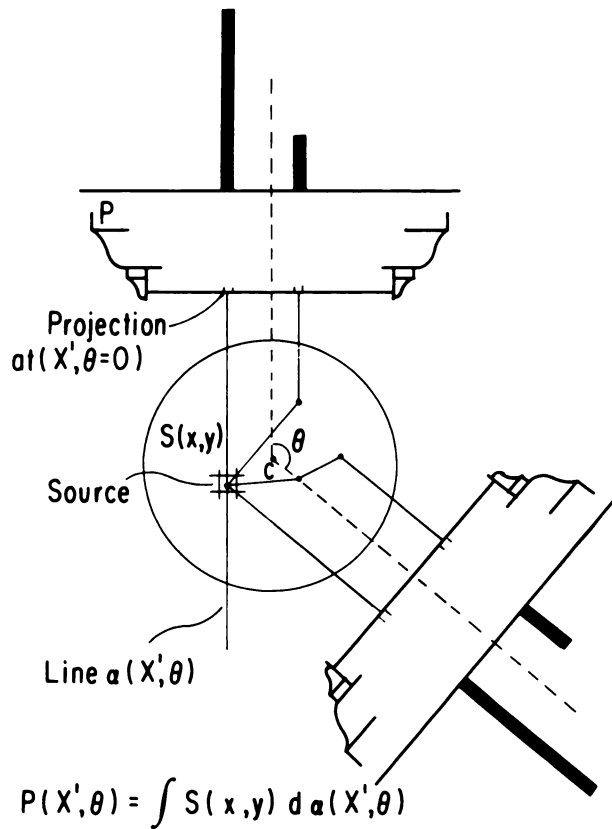
FIGURE 1
Filtered backprojection model of SPECT projection. Required assumption of line integral

have penetration and real detectors have finite spatial resolution resulting in spreading of the tails of a point source response. A 140-keV photon flux from technetium-99m originating at the center of a water filled cylinder of 11 cm radius will experience attenuation of ~80%. For every 100 photons which are not attenuated, there will be an additional unwanted contribution of 32 photons due to scattering.

There is then a discrepancy between the idealized model of ECT required by FBP and the reality of practical data acquisition. IMOC is presented as a reconstruction algorithm which is based on a more realistic model of the SPECT process.

Technique

The acquisition of projection profiles in SPECT is a sampling of the photon flux distribution at the plane of the gamma camera due to a distributed radioactive photon source located in a scattering and attenuating medium and thus the observed projections may be represented by solutions to a photon transport equation (23,24). Given a source distribution, solution of the transport equation yields projection data. We desire to solve the inverse problem: given the projection data, find the source distribution. Based on a Monte Carlo model which has been shown to successfully model the SPECT imaging system (25-27), the reconstruction
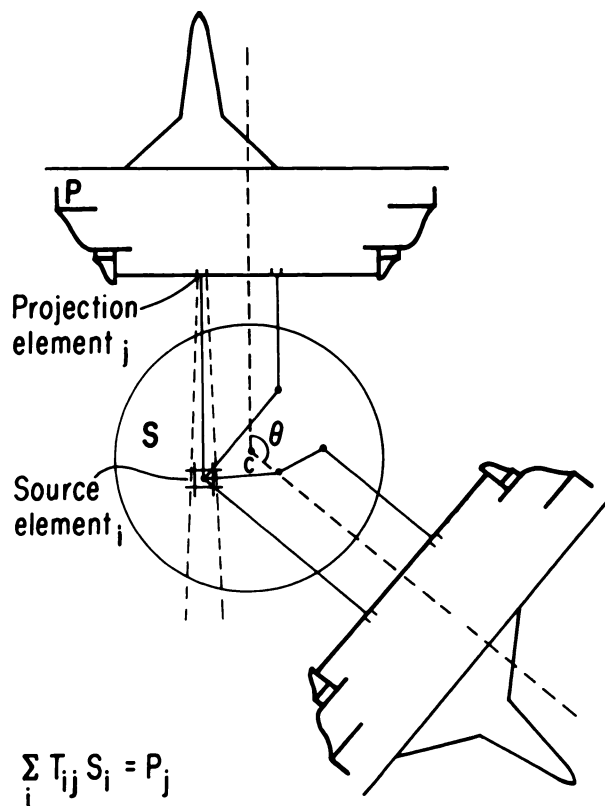
rely on empirical parameterizations. The parameters used will depend not only on the physical properties of the acquisition, but even on the order in which the compensations are applied. Attenuation compensation typically is applied with parameter values which compensate partially for scatter (3,4), and thus will require different parameter values if the data has been scatter compensated. The empirical scatter and attenuation parameters will depend partially on characteristics of the acquisition system such as energy resolution and must be experimentally determined at each application site. These are not reasons to dismiss the sequential compensation techniques, but do provide motivation for seeking a unified algorithm which implements the scatter and attenuation information simultaneously with the reconstruction process. A unified reconstruction algorithm will estimate a source pixel activity based on simultaneous consideration of all projection elements which can contribute to the source pixel and will include in this consideration the effects of scatter, attenuation, and collimator divergence.

A more realistic picture of SPECT photon acquisition from a distributed source in an interacting medium is shown in Fig. 2. Collimator holes are of finite length and diameter and thus have an acceptance defined by a cone (shown by the dashed line). Real collimators

$$\sum_i T_{ij} S_i = P_j$$

FIGURE 2
Inverse Monte Carlo model of SPECT projection assumes more realistic model

problem is solved using inverse Monte Carlo (28,29). Physical characteristics of the acquisition apparatus (such as energy window setting, system energy and spatial resolution, and radius of rotation) as well as of the body (such as contour and density) are incorporated in the Monte Carlo model. Note that this model does not presuppose any preknowledge of the actual source distribution but does suppose knowledge of the scattering medium boundary (body outline). The ECT acquisition system is modeled using Monte Carlo techniques resulting in a system of linear equations relating the radiopharmaceutical distribution to the measured ECT projection data. This linear system is solved to yield the radiopharmaceutical distribution. Algebraically, the ECT reconstruction problem may be written as follows. Given a radionuclide source element S_i, the projected photon flux density P_j measured in a detector pixel $j(r,o)$ may be written:

$$P_j = T_{ij}S_i, \tag{1}$$

where T_{ij} is a matrix of the probability of a photon which originated in source element S_i to be observed in detector element P_j. The ECT reconstruction problem is to estimate S_i given P_j. A flow chart of the IMOC algorithm is shown in Fig. 3. Using the Monte Carlo model, accurate estimates of T_{ij} can be computed for a source voxel i. Since the system will typically be over-determined (more equations than unknowns), and will not have an exact solution due to instrumental and statistical errors in the projection data, a minimum variance solution is sought using the EM algorithm for Maximum Likelihood estimation (30,31).

The reconstructed images were evaluated with criteria appropriate to the imaged object. Uniform activity regions were compared by evaluating a percent root-mean-square (%RMS) noise value. Resolution recovery was determined for the line source images by computing full widths at half maximum (FWHM) for a slice through the image. The full widths were computed by first order linear interpolation. For the cold defect phantom, an image contrast factor was computed. Projection data were acquired on the Duke SPECT system (32) with 0.32 cm/pixel spatial sampling and 2° per projection continuous angular sampling. Slice thickness was 1.7 cm. Where 4° or 8° angular sampling is quoted, 2° projections were summed to generate the desired angular sampling. The studies were performed using technetium-99m (^{99m}Tc) and data were acquired using a 20% energy window symmetrically centered at 140 keV. A high resolution collimator was used. A circular orbit was maintained with a radius of rotation of 14 cm. Projection data were flood corrected for camera non-uniformity and decay corrected. Scan times were typically 22 min. The phantom* provides an 11 cm radius cylinder 27 cm long.
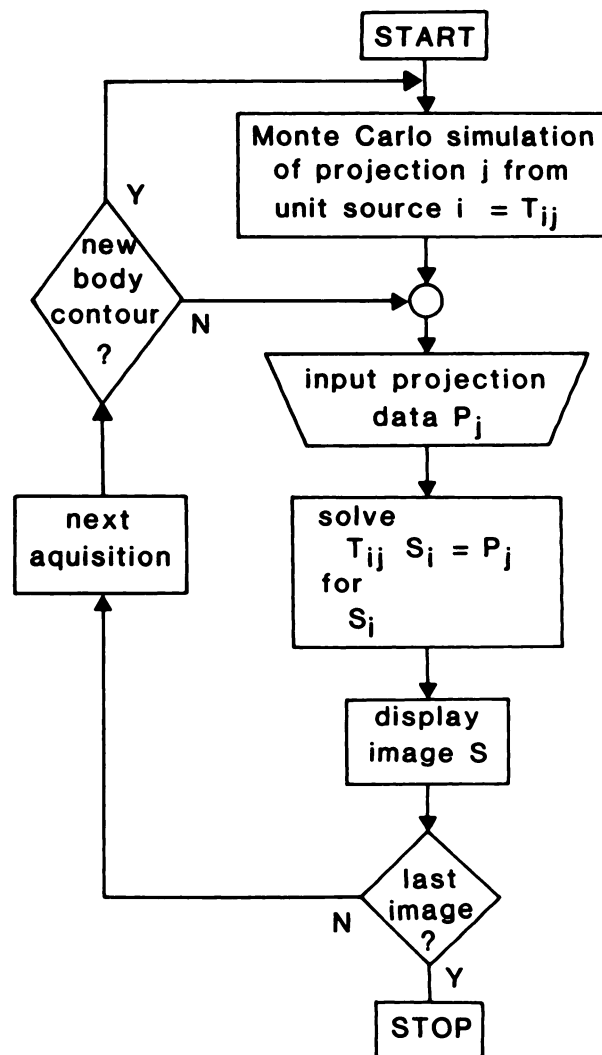

FIGURE 3
Flow chart of the Inverse Monte Carlo algorithm.

The filtered backprojection was performed using a ramp filter modified by a generalized Hanning window (15). The Hanning window rolloff frequency will be expressed as a fraction of the Nyquist frequency (1.56 cm⁻¹ for the 0.32 cm sampling). Attenuation compensation for the FBP was achieved using the zeroth order multiplicative algorithm of Chang (21) with an interaction coefficient of 0.12 cm⁻¹ (33). This coefficient value provides a limited compensation for scatter.

RESULTS

Results for Inverse Monte Carlo (IMOC) reconstructions are presented here. Representative results for FBP are included for comparison but no attempt is made to thoroughly and quantitatively evaluate the comparison. No scatter compensation has been applied to the FBP

images which follow except for the use of 0.12 cm⁻¹ as an interaction coefficient in the Chang attenuation compensation.

A central slice through reconstructed images of a uniform cylinder is shown in Fig. 4. The relative effects of scatter and attenuation compensation may be seen in Part A for IMOC. Ideal reconstruction of the uniform cylinder will be flat. The reconstruction with no compensation shows the expected dip in the center due to increased attenuation. When compensation is made for attenuation only, the overall counts are increased and the image is increased in the center. Compensation for scatter removes this central increase and decreases the total counts. Part B of Fig. 4 shows similar results for FBP. An improvement in reconstructed image noise is apparent for IMOC.

The cylindrical phantom containing a uniform distribution of ^{99m}Tc was scanned several times with a range of activities to evaluate the behavior of the algorithm with projection data containing different statistical noise contributions. The total counts in the projection sets ranged from 10^5 to 1.4×10^7. A rolloff frequency of $0.7f_N$ was chosen for the FBP filter. Images were reconstructed with 0.32 cm/pixel spatial sampling and 8° angular sampling. Representative images along

FIGURE 4
Central slice through reconstructed uniform cylinder for A) IMOC showing effect of attenuation and scatter compensation B) FBP

with profiles (width = 1 pixel) are shown in Figs. 5 and 6. The improvement in noise for IMOC is apparent. The results are presented graphically in Fig. 7 where the %RMS as a function of total counts in the projection set is plotted on a semilog scale. The solid circles are the FBP results while the open circles are the IMOC results. The solid curves are predictions using an analytic expression (34) for noise propagation through the FBP algorithm. There is a separate curve for each filter rolloff. The solid circles follow the $0.7f_N$ curve very well. From this figure we see the IMOC points follow a similar curve as a function of counts but have a lower %RMS content; however, a word of caution is in order. As the number of iterations is increased with the EM estimator, the noise will increase also. Since the IMOC was initialized with a constant uniform source activity, convergence was rapid and convergence (as determined by a chi-squared test) was obtained after only four iterations. This dependence of noise on number of iterations along with the dependence of convergence rate on object content (35) implies that a uniform cylinder may be a deceptively simple test for IMOC.

In a typical clinical image there will be structural information and the image will be interpreted by a combination of its resolution recovery and noise. To evaluate these factors in the reconstructed image, five ^{99m}Tc line sources were placed in the cylinder containing ^{99m}Tc and water. Reconstruction of this phantom was evaluated by %RMS in the uniform area and the FWHM of the line sources. Results are shown plotted in Fig. 8 as %RMS versus FWHM for FBP (solid circles) and IMOC (open circles) where the number near the open circle gives the number of iterations and the number beside the solid circle gives the filter rolloff frequency. The FBP shows expected behavior; as the rolloff frequency is decreased, the resolution is degraded while the noise is reduced. With IMOC, as the number of iterations is increased from 4 to 20 the resolution improves and the noise is reduced (although the noise remains higher than the value obtained with the same uniform concentration without the line sources). After ~20 iterations, however, the %RMS begins to increase while the FWHM continues to decrease. This is in contrast to the results for the uniform cylinder alone where the noise increased monotonically with iteration, confirming that the convergence behavior is dependent on the information content in the image. When starting with a uniform estimate of the activity, the algorithm will converge much more quickly for a uniform source distribution than for a more complex distribution.

Scatter and attenuation compensation were evaluated by reconstructing scans of line sources in air and in water. With proper compensation, the image of lines in water should reconstruct with same intensities as those same lines scanned in air. Regions of interest were
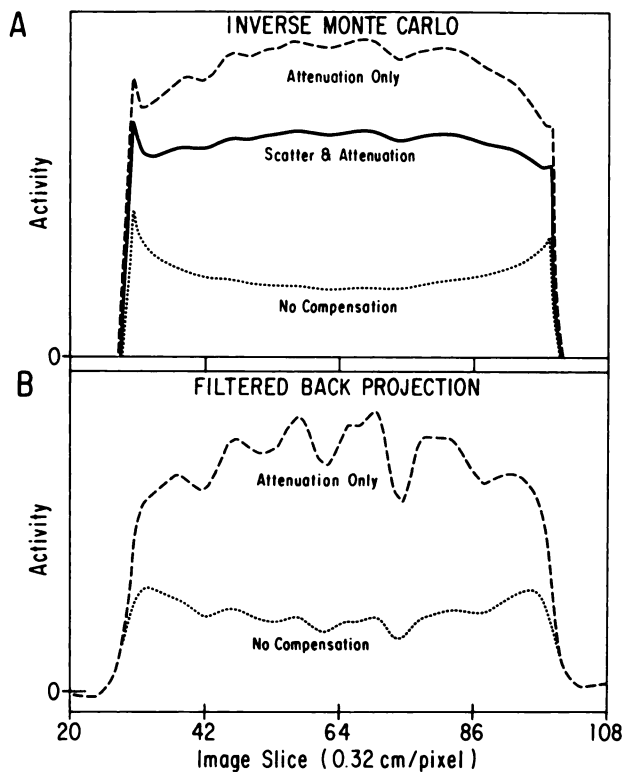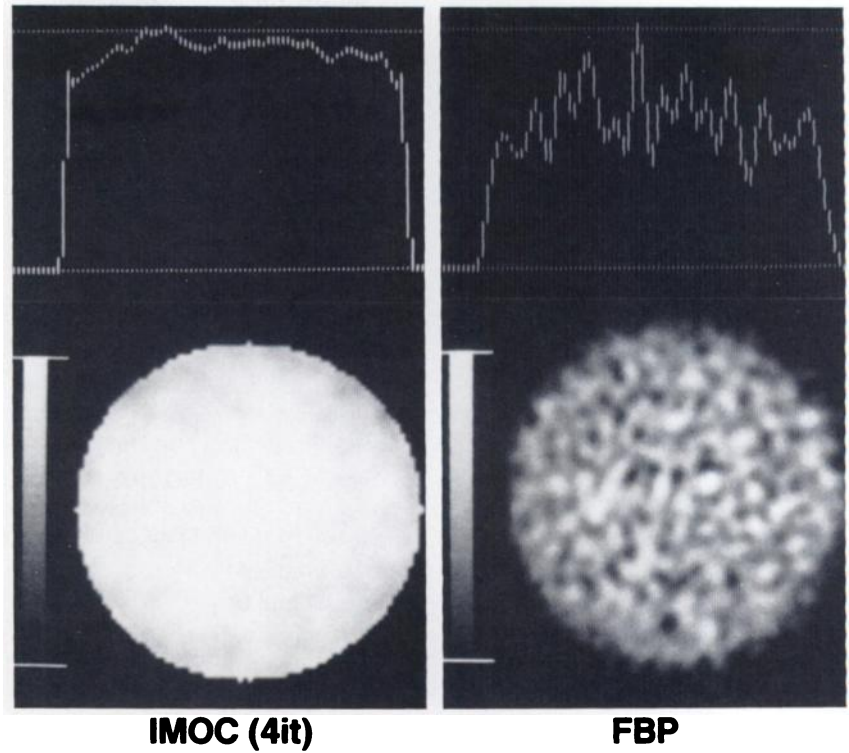
IMOC (4it)   **FBP**

FIGURE 5
Reconstruction of uniform cylinder: 70,000 counts in projections. IMOC on left, FBP on right

set around the line image maximum and the values are shown in Fig. 9 for IMOC. There is excellent agreement between the compensated scan in water and the scan in air verifying the simultaneous compensation for scatter and attenuation provided by the IMOC algorithm.

While the line source in water phantom provides a quantitative test for scatter and attenuation compensation, a more difficult test is provided by a nonradioactive defect surrounded by radioactivity. This test reflects an important application of SPECT imaging; the detec-
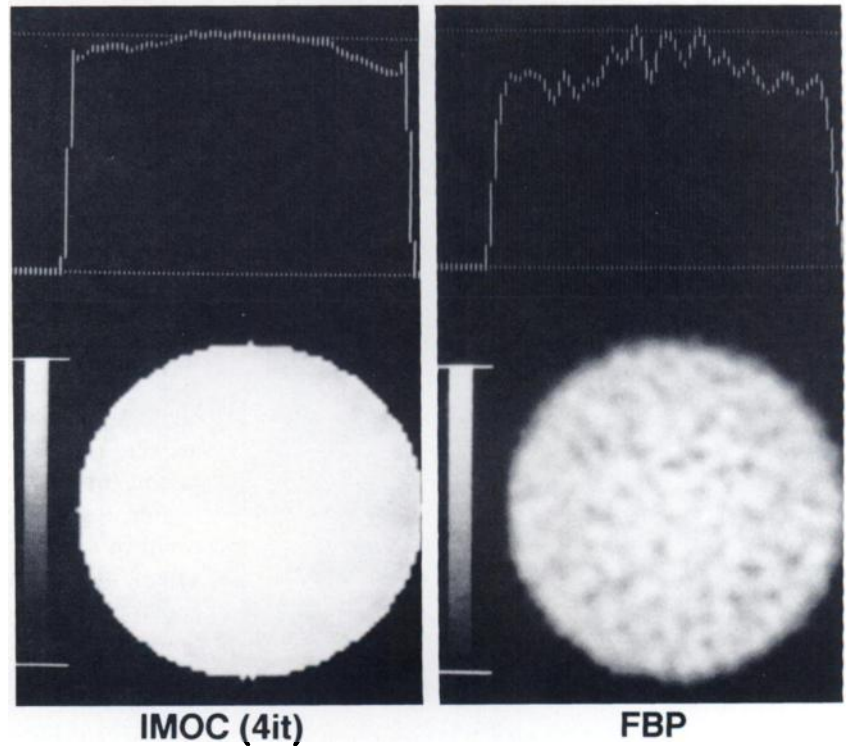
390 COUNTS

IMOC (4it)   **FBP**

FIGURE 6
Reconstruction of uniform cylinder: 391,000 counts in projections. IMOC on left, FBP on right
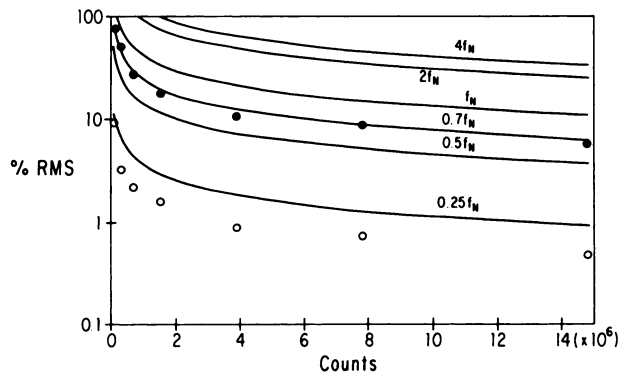
FIGURE 7
Image noise for uniform cylinder phantoms. Results for four iterations of IMOC compared with FBP results

FIGURE 9
ROI analysis of line sources in water phantom showing scatter and attenuation compensation for IMOC

tion of lesions in clinical liver scans. A measure of the detectability of lesions is provided by the image contrast which will vary between −1 for optimal contrast and 0 for minimal contrast. The presence of scatter will decrease the image contrast (*17,22*) as will effects due to finite system resolution (*14*). A cold sphere phantom (6 cm diameter nonradioactive sphere placed in the cylindrical phantom filled with radioactivity) was imaged to evaluate the contrast recovery of the IMOC algorithm. Results for this cold sphere phantom were disappointing. The FBP reconstruction had a contrast of −0.77 ± 0.07 which could be improved to ⁻0.97 using techniques of Ref. (*22*). Forty iterations of IMOC were required to obtain contrast of ⁻0.76 ± 0.05. One hundred iterations obtained ⁻0.89 ± 0.17 but with increased uncertainty. An asymptotic test using a similar phantom and an array processor obtained ⁻0.97 ± 0.2 at 500 iterations requiring 25 min of computation time. Although the IMOC reconstruction represents the defect more accurately than the FBP, convergence was disappointingly slow.

Two human brain studies were reconstructed with compensation for attenuation and scatter. A recon-
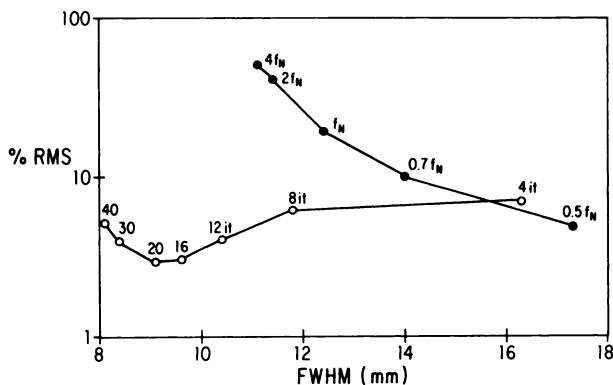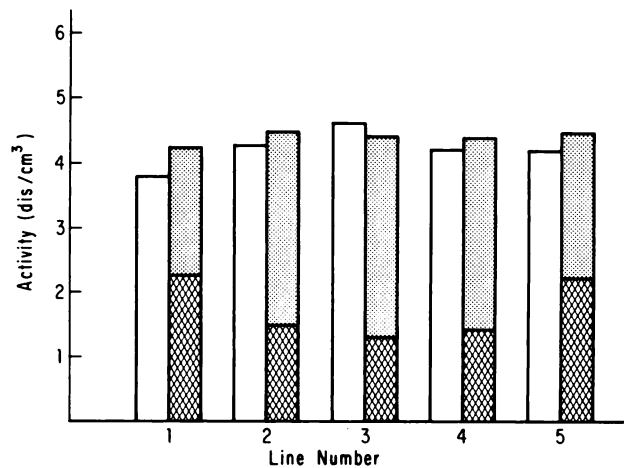
structed image of a [^{99m}Tc] red cell blood-pool study is shown in Fig. 10. The left side shows the IMOC reconstruction while the right side shows an FBP reconstruction with a Hanning window rolloff frequency of 0.7 F_n, a value which produced the most visually satisfying FBP image and one typically used for clinical scans. The total counts in the projection set was 326,000 and 24 iterations were performed. Higher contrast and superior resolution are seen in the IMOC image. Both images were normalized to the highest pixel value. For this blood-pool study the largest value occurred in the sagittal sinus—not a region of clinical interest. The superior resolution of the IMOC reconstruction results in this narrow object having a higher value above the regions of interest than for the FBP. The resulting depression of these lower lying regions which are of interest complicates visual comparison of the two images. To facilitate comparison in the interesting region, profiles are shown above each image. The improvement in noise and resolution characteristics for IMOC are evident. A [^{99m}Tc]glucoheptonate brain study is shown in Fig. 11 with IMOC to the left, FBP to the right and with a profile shown above each. The improvement in resolution and decreased noise provided by IMOC allow finer detail to be distinguished in the low activity regions. Total counts in the projections were 165,000 and 40 iterations were performed. Both of these brain studies were reconstructed assuming the cylindrically symmetric, uniformly attenuating, and scattering source region described above. While this assumption will result in some error in the quantitative reconstructed values, it is encouraging to note that the reconstructed activity distribution has a correct noncircular shape and that no serious artifacts were introduced by this assumption even when the actual source distribution extended outside the modeled source region as in the labeled cell study.
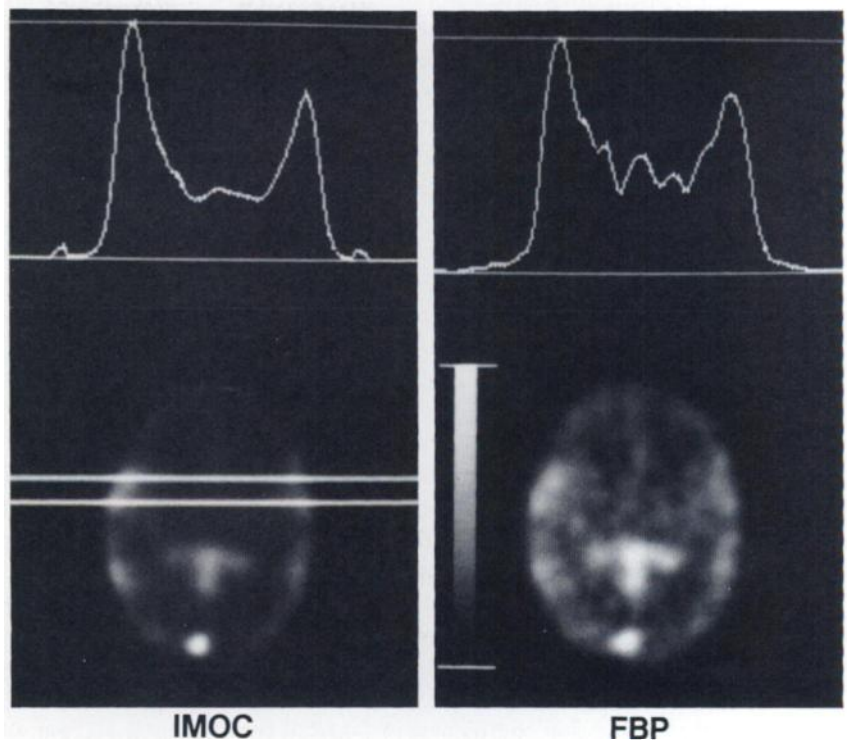

FIGURE 8
Resolution and noise for line source in uniform activity

FIGURE 10
^{99m}Tc-labeled red blood cell blood-pool study for brain. IMOC on left, FBP on right

IMOC   FBP

DISCUSSION

Inverse Monte Carlo (IMOC), a new reconstruction algorithm for SPECT, is presented based on a detailed physical model of the SPECT data acquisition process. Monte Carlo techniques are employed to model the system and an estimate of the source distribution is made using a maximum likelihood EM estimator. Compensation is provided simultaneously for scatter and attenuation as well as for collimator divergence since these effects are included in the transformation
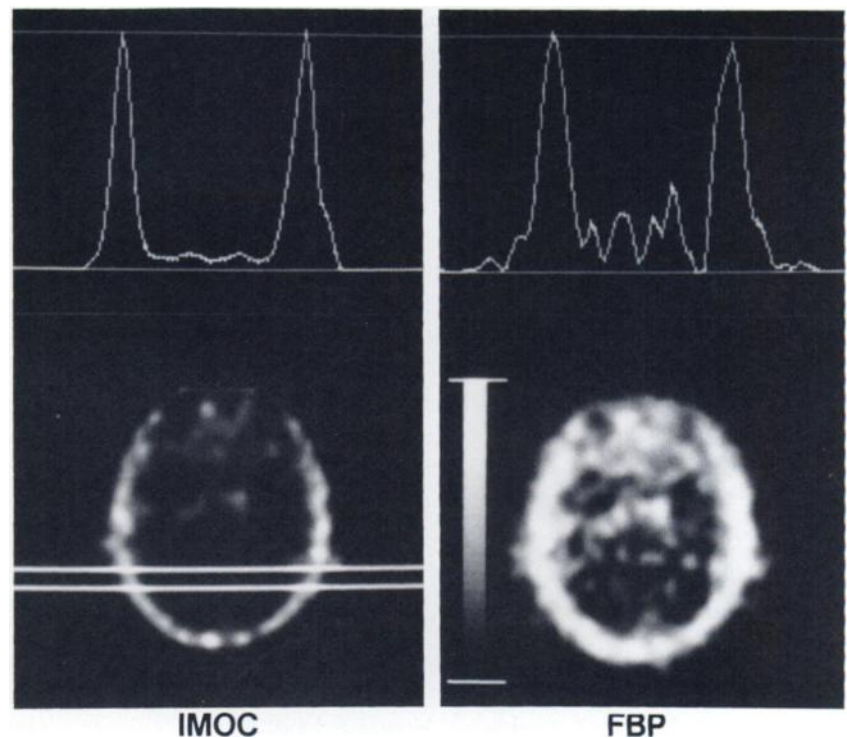

FIGURE 11
[^{99m}Tc]glucoheptonate scan of brain. IMOC on left, FBP on right

IMOC   FBP

probability matrix. It is important to note that these compensations are performed without the need for empirical parameter input such as the modified attenuation coefficient and scatter fraction (17–22) values required for most attenuation and scatter compensations. Instead, intrinsic parameters of the acquisition system such as energy resolution and collimator dimensions are used in the Monte Carlo calculations. IMOC reconstructions of experimental projection data were presented along with filtered backprojection reconstructions for phantom as well as clinical studies. Rate of convergence (number of iterations required) for the iterative IMOC algorithm was shown to be source object dependent. Convergence (number of iterations required for a stable solution) was faster for hot sources in a cold background than for cold regions in an active background. This nonlinear behavior is an important feature of the iterative EM maximum likelihood reconstruction algorithm and is a serious concern for further study. For simple objects and high counting statistics where each projection is unambiguous, convergence is rapid. Where there is considerable ambiguity between projections (as with small cold defects and/or high noise in the projections) convergence will be slower. Preliminary investigations indicate that the recovery of spatial frequency information is achieved at different numbers of iterations for different spatial frequencies; higher spatial frequencies appear at higher iterations while the lower frequencies (smooth structure) are well defined at early iterations. Compared with FBP, IMOC reconstructions contained less noise and had better resolution. Although scatter compensation was not included in the FBP reconstructions, the sequential scatter compensation techniques available (17,20,22) involve subtraction of counts and will increase the FBP image noise. Successful simultaneous compensation for scatter and attenuation was demonstrated for IMOC. A cold defect in an active region required a disappointing number of iterations to achieve only a modest image contrast. Two clinical human brain studies were reconstructed providing visually superior images.

The most dramatic improvements using IMOC are apparent for those studies with few photon events. This is significant since clinical SPECT studies are usually count limited. This improvement in image noise is believed due to several features of IMOC: the incorporation into the EM algorithm of the knowledge that the photon counting process follows a Poisson distribution, the simultaneous solution approach, and that detailed modeling provided by the Monte Carlo estimation which reduces the inconsistency in the equations. The most effective clinical implementation of IMOC in its present state of development appears to be in studies where the signal to noise ratio is too low for conventional FBP reconstruction. Specific applications include iodine-123 HIPDM brain studies using high resolution, low sensitivity collimation. The improved resolution and noise handling characteristics of IMOC should provide higher quality, high resolution images.

Another promising application may be thallium-201 imaging of the heart where standard techniques have resulted in high noise reconstructions. At present, the algorithm does not appear to provide great improvement for cold defect imaging such as required for liver tumor detection. This latter deficiency is not fully understood and is a focus for future research.

The most obvious disadvantage of the IMOC algorithm is the increased computation effort required to reconstruct an image. The IMOC images shown here were reconstructed into an image plane consisting of 4,020 pixels of width 3.2 mm. The computer time used for the Monte Carlo modeling is proportional to the number of image pixels reconstructed and was ~10 hr on a VAX 11/780 minicomputer for the work shown although reasonable results can be obtained in 4 hr. For 3.2 mm sampling at 45 angles, the EM step required 0.5-hr per iteration.

The clinical images shown were achieved with ~50 iterations or 25 hr. The EM step required 0.5 hr per iteration. It should be recognized that the reconstruction times presented here were obtained from developmental software and by no means represent optimal algorithm performance. Preliminary investigation using pipelined hardware (MAP 6420, CSPI) for the limited case of 6.3 mm sampling at 36 angles resulted in reconstruction times of 2 sec per iteration for the EM step. Thus a clinical image could be reconstructed (20 iterations) in under 1 min.

Much work remains to fully refine and evaluate IMOC as a clinically viable reconstruction algorithm for SPECT. While theoretically pleasing, the EM algorithm is only one way to solve the system of equations. Alternatives include iterative least squares (36), conjugate gradient (37), maximum entropy (38), eigenvalue decomposition (39), simulated annealing (40), ART (8–10,12) and SIRT (11). Some combination of these, utilizing the accurate system modeling provided by Monte Carlo, will hopefully result in a reconstruction algorithm for SPECT with simultaneous compensation for attenuation and scatter which is versatile and rapid enough for routine clinical use. The preliminary results presented here demonstrate that the development of IMOC providing simultaneous scatter and attenuation compensation is a major step toward the realization of quantitative SPECT.

FOOTNOTE

ACKNOWLEDGMENTS

REFERENCES

1. Radon J: Uber die bestimmung von funktionen durch ihre integralwerte langs gewisser manningfaltigkeiten. *Ber Verch Sachs Akad Wiss* 69:262–277, 1917.
2. Bracewell RN: Strip integration in radio astronomy. *Aust J Phys* 9:198–217, 1956
3. Kuhl DE, Edwards RQ: Image separation radioisotope scanning. *Radiology* 80:653–662, 1963
4. Kuhl DE, Edwards RQ: Cylindrical and section radioisotope scanning of the liver and brain. *Radiology* 83:926–935, 1964
5. Shepp LA, Logan BF: Reconstructing interior head tissue from x-ray transmissions. *IEEE Trans Nucl Sci* NS-21:228–236, 1974
6. Ramachandran GN, Lakshminarayanan AV: Three dimensional reconstruction from radiographs and electron micrographs: Application of convolutions instead of Fourier transforms. *Proc Natl Acad Sci USA* 68:2236–2240, 1971
7. Kay DB, Keyes Jr JW, Simon W: Radionuclide tomographic image reconstruction using Fourier transform techniques. *J Nucl Med* 15:981–986, 1974
8. Herman GT and Lent A: Iterative reconstruction algorithms. *Comput Biol Med* 6:273–294, 1976
9. Herman GT, Lent A, Rowland SW: ART: mathematics and applications. *J Theor Biol* 42:1–32, 1973
10. Herman GT, Lent A, Lutz PH: Relaxation methods for image reconstruction. *Commun ACM* 21:152–158, 1978
11. Gilbert P: Iterative methods for the three-dimensional reconstruction of an object from projections. *J Theor Biol* 36:105–117, 1972
12. Gordon R, Bender R, Herman GT: Algebraic reconstruction techniques (ART) for three-dimensional electron microscopy and x-ray photography. *J Theor Biol* 29:471–481, 1970
13. Jaszczak RJ, Coleman RE, Lim CB: SPECT: Single photon emission computed tomography. *IEEE Trans Nucl Sci* NS-27:1137–1153, 1980
14. Whitehead FR: Quantitative analysis of minimum detectable lesion-to-background uptake ratios for nuclear medicine imaging system. In *International Atomic Energy Agency, Vienna,* 409–434, 1977
15. Jaszczak RJ, Coleman RE, Whitehead FR: Physical factors affecting quantitative measurements using camera-based single photon emission computed tomography (SPECT). *IEEE Trans Nucl Sci* NS-28: 69–80, 1981
16. Floyd CE, Jaszczak RJ, Coleman RE: Inverse Monte Carlo: A unified reconstruction algorithm for SPECT. *IEEE Trans Nucl Sci* NS-32:779, 1985
17. Floyd CE, Jaszczak RJ, Coleman RE: Deconvolution of Compton scatter in SPECT. *J Nucl Med* 26:403–408, 1985
18. Walters TE, Simon W, Chesler DA, Correia JA: Attenuation correction in gamma emission computed tomography. *J Comput Assist Tomogr* 5:89–94, 1981
19. Gullberg CT, Budinger TF: The use of filtering methods to compensate for constant attenuation in single-photon emission computed tomography. *IEEE Trans Biomed Eng* BME-28:142–157, 1981
20. Axelsson B, Msaki P, Israelsson A: Subtraction of Compton-scattered photons in single-photon emission computerized tomography. *J Nucl Med* 25:490–494, 1984
21. Chang LT: A method for attenuation correction in radionuclide computed tomography. *IEEE Trans Nucl Sci* NS-25:638–642, 1978
22. Jaszczak RJ, Greer KL, Floyd Jr CE, et al: Improved SPECT quantitation using compensation for scattered photons. *J Nucl Med* 25:893–900, 1984
23. *Nuclear Reactor Theory,* Bell G, Glasstone S. Van-Nostrand-Reinhold, 1970
24. *Computational Methods of Neutron Transport,* Lewis EE, Miller WF. New York, John Wiley and Sons, 1984
25. Beck JW: Analysis of a Camera Based Single Photon Emission computed tomography (SPECT) System. PhD Dissertation, 1982 Duke University, (University Microfilms) Ann Arbor, Michigan
26. Beck JW, Jaszczak RJ, Colemen RE, et al: Analysis of SPECT including scatter and attenuation using sophisticated Monte Carlo modeling methods. *IEEE Trans Nucl Sci* NS-29:506, 1982
27. Floyd CE, Jaszczak RJ, Harris CC, et al: Energy and spatial distribution of multiple order Compton scatter in SPECT: A Monte Carlo investigation. *Phys Med Biol* 29:1217–1230, 1984
28. Dunn WL: Inverse Monte Carlo analysis. *J Comput Phys* 41:154–166, 1981
29. Dunn WL: Inverse Monte Carlo solutions for radiative transfer in inhomogeneous media. *J Quant Spectrosc Radiat Trans* 29:19–26, 1983
30. Shepp LA, Vardi Y: Maximum likelihood reconstruction for emission tomography. *IEEE Trans Med Imag* MI-1:113–122, 1982
31. Lange K, Carson R: EM reconstruction algorithms for emission and transmission tomography. *J Comput Assist Tomogr* 8:306–316, 1984
32. Greer KL, Jaszczak RJ, Coleman RE: An overview of a camera-based SPECT system. *Med Phys* 9:455–463, 1982
33. Harris CC, Greer KL, Jaszczak RJ, et al: Tc-99m attenuation coefficients in water-filled phantoms determined with gamma cameras. *Med Phys* 11:681–685, 1984.
34. Jaszczak RJ, Greer KL, Floyd CE, et al: Estimating SPECT count densities, scatter fractions, and statistical noise. *IEEE Trans Nucl Sci* NS-32:762–768, 1985
35. Rockmore AJ, Macovski A: A maximum likelihood approach to transmission image reconstruction from projections. *IEEE Trans Nucl Sci* NS-24:1929–1935, 1977
36. Budinger TF, Gullberg GT: Three-dimensional reconstruction in nuclear medicine emission imaging. *IEEE Trans Nucl Sci* NS-21:2–20, 1974
37. Kawata S, Nalcioglu O: Constrained iterative reconstruction by the conjugate gradient method. *IEEE Trans Med Imag* MI-4:65–71, 1985
38. Minerbo G: Maximum entropy reconstruction from cone-beam projection data. *Comput Bio Med* 9:29–37, 1979
39. Llacer J: Tomographic image reconstruction by eigenvector decomposition: Its limitations and areas of applicablity. *IEEE Trans Med Imag* MI-1:34–42, 1982
40. Smith WE, Barrett HH, Paxman RG: Reconstruction of objects from coded images by simulated annealing. *Opt Lett* 8:196, 1983